

Near-Infrared Speckle-Illumination Imaging Based on a Multidimensionally Disordered Fiber Laser

Zhao Wang,¹ Shanshan Wang,¹ Rui Ma¹, Youwei Liu¹,¹ Hongyang Zhu,¹ Yong Zhang,¹ Jun Liu,² Yandong Mu,³ Yunjiang Rao,^{1,*} and Weili Zhang^{1,†}

¹*Fiber Optics Research Centre, School of Information and Communication Engineering, University of Electronic Science & Technology of China, Chengdu 611731, China*

²*International Collaborative Laboratory of 2D Materials for Optoelectronics Science and Technology of Ministry of Education, Institute of Microscale Optoelectronics, Shenzhen University, Shenzhen 518060, China*

³*Medical School, University of Electronic Science & Technology of China, Chengdu 611731, China*

(Received 13 April 2022; revised 28 June 2022; accepted 5 July 2022; published 10 August 2022; corrected 26 August 2022)

Speckle illumination is extensively applied in various imaging scenarios due to its advantages in enhancing the performance of imaging. Generally, the existing speckle-illumination methods are mainly based on external spatial modulation of light through a rotating diffuser or spatial light modulator. Both the lighting efficiency and the system's compactness are limited for these conventional external modulation methods, due to their free-space light coupling and insertion or diffraction loss. Here, a multimode fiber laser with self-reconfigurable speckle illumination is proposed and realized, benefiting from the temporal-spectral randomness of a homemade coherent random-fiber laser and the spectral-sensitive output pattern of an out-coupling multimode fiber. Output characteristics in the spectral and spatial domain of the proposed laser are analyzed and show dynamically varying speckles within a moderate bandwidth. These features pave efficient ways for superresolution imaging through an opaque scattering medium as well as ghost imaging, which is realized and demonstrated based on the lighting of the proposed laser.

DOI: 10.1103/PhysRevApplied.18.024031

I. INTRODUCTION

Spatially designed illumination plays a pivotal role in breaking through the imaging limitation and realizing high imaging quality (e.g., resolution and contrast) for advanced imaging systems. In stimulated emission-depletion microscopy, a doughnut beam is essential to deplete the excited-state photons and shrink the point-spread function (PSF) to reach superresolution imaging [1]. In structured illumination microscopy, the high-frequency information of the object is transferred into the frequency-response range of the optical transfer function by employing sinusoidal-structured light [2].

As one emerging method of spatially designed illumination, laser speckle illumination (LSI), which uses uncorrelated patterns of laser fields, is extensively studied due to its great significance to improve the imaging capability. Superresolution imaging is reported using various LSI methods, such as speckle-saturated fluorescence excitation [3], customized speckle for photoswitching [4], blind-structured illumination microscopy [5],

scattering-assisted imaging [6], and photoacoustic fluctuation imaging [7]. Additionally, the uncorrelated LSI is also crucial in realizing spatial-domain ghost imaging with advantages of nonlocality, antiturbulence, and anti-interference [8–10]. Currently, laser speckles are mainly generated by two ways of external modulation. The first one uses a time-variant diffuser, such as rotating ground glass, to disturb the output of a relatively narrow linewidth laser, which is easy to be implemented at a low cost [11–13]. The other one forms disordered laser patterns using a spatial light modulator (SLM), which is programmable and highly controllable [3,4,14,15]. However, both ways use free-space coupling, which limits the compactness of the system and suffers from low lighting efficiency due to nondirectional scattering and inevitable insertion or diffraction loss.

With the advantages of a compact all-waveguide structure, low transmission loss, and wide operating bandwidth, multimode-fiber- (MMF) integrated light sources can efficiently generate speckle patterns originating from interference of its transverse modes. The spectral decorrelation bandwidth of MMF-generated speckles can be extremely narrow, which is successfully applied to a high-resolution spectrometer and wavelength-dependent speckle multiplexing for phase-retrieval imaging [16–18]. However,

*yjrao@uestc.edu.cn

†wl_zhang@uestc.edu.cn

conventional MMF-integrated light sources generate only fixed speckle patterns due to the fixed operating wavelength. The uncorrelated speckles are generally realized by external modulation, such as changing the fiber state and tuning the injected lasing wavelength. Therefore, it is necessary to promote a MMF-based LSI technique with inherently automodulated speckle generation, which is applicable for different scenarios of LSI imaging.

On the other hand, coherent random lasers with dynamically varying spectra show promising advantages in speckle-free imaging, sensing, and information encryption [19,20]. Benefiting from the randomly and sparsely distributed lasing spikes of a coherent random laser, superresolution spectroscopy is realized [21], which opens up perspectives for random lasing-based applications. Exploiting the advantages of the complex output characteristics of random lasers is of great significance.

Here, an all-fiber random laser is proposed by combining the spectral disorder of random lasing and the decorrelated speckle formation in the MMF, developing the so-called multidimensionally disordered fiber laser (MDFL) that features complex output characteristics in the spectral, spatial, and temporal domains. The laser employs randomly distributed coherent feedback from several weakly reflective Fabry-Perot cavities in combination with a MMF. It emits a sparse spectrum, varying wavelengths, and multiple transverse modes, which lead to the formation of dynamic, high-contrast, and spatially uncorrelated speckle patterns. Such multidimensional randomness perfectly satisfies the requirement of speckle-illumination imaging, through which superresolution imaging and ghost imaging through an opaque scattering medium are realized. The reconstructed results indicate that both imaging scenarios exhibit excellent performance using the MDFL. The proposed imaging method has the advantages of self-modulated random speckle generation, a compact all-fiber illumination structure, and high lightening efficiency at near-infrared wavelength, which is of great significance for the development of advanced speckle-illumination imaging.

II. CHARACTERISTICS OF THE DISORDERED FIBER LASER

In traditional LSI, the spatiotemporally varying speckles are generated through modulating a time-variant diffuser or SLM, as shown in Figs. 1(a) and 1(b). Apart from the above methods, a MMF is also promising for forming speckle patterns, as it provides abundant transverse modes and mode crosstalk induced by microbending and defects. Generally, the sizes of generated speckle grains are determined by the number and weight of transverse modes in the MMF [22]. Interestingly, the speckles are also strongly dependent on the wavelength of light, e.g., ultranarrow spectral decorrelation bandwidth can be obtained with a

sufficient length of MMF [16], which is ideal for dynamic speckle generation. Therefore, the idea of our MDFL is to realize random wavelength emission (coherent random lasing) in the MMF for generating self-modulated and low-insertion-loss speckle patterns, as shown in Fig. 1(c). It is worth noting that low insertion loss here refers to the speckle-generation and illumination part (i.e., the MMF) rather than the laser-generation part, which is compared with the SLM approach and the rapidly rotating ground-glass approach.

The experimental setup of the MDFL is shown in Fig. 1(d). The feedback element is a random array of Fabry-Perot cavities that is realized by depositing a thin gold film on 11 end facets of FC-PC-type fiber pigtail and connecting them in series. The distances between two neighboring FC-PC-type fiber pigtailed are randomly distributed from 0.43 to 3.87 m. A photograph of the gold-deposited FC-PC-type fiber pigtail and RDFFPs is shown in Fig. S1 within the Supplemental Material [23]. Each of the gold-deposited FC-PC-type fiber pigtailed has a reflectivity of 5%, providing wavelength-independent coherent random feedback. A 980-nm pump laser is launched into the ring cavity through a 980/1550 wavelength-division multiplexer (WDM). A 14-m-long erbium-doped fiber (EDF, EDFC-980-HP, Nufern) works as the gain medium to reduce the lasing threshold and obtain stronger stimulated emission light. The array of Fabry-Perot cavities is introduced into the configuration by employing a circulator that forces light flow unidirectionally, i.e., light injected from port 1 will be directionally coupled into port 2, and light reflected by the array of Fabry-Perot cavities or injected from port 2 will be directionally coupled into port 3. The laser output is coupled out of the ring cavity using a 50:50 coupler. A polarization controller is used to flexibly adjust the statistical bandwidth of random lasing. This is because the optical circulator is polarization dependent, and it partially controls the reflection spectrum of the RDFFPs together with the polarization controller. A photograph of the actual experimental setup is shown in the Fig. S2 within the Supplemental Material [23].

Figure 1(e) gives the reflection spectrum of the array of Fabry-Perot cavities, which shows randomly distributed spikes (eigenmodes) over a wide range of wavelengths. Due to a large number of eigenmodes existing within the gain profile of the EDF, strong competition between resonant modes will disturb the output spectrum. The relationship between pump and output power is shown in Fig. 1(f), where the lasing threshold is about 10 mW. Beyond the threshold, the output power increases linearly with the pump power, which is a typical characteristic of laser emission. The output is further injected into a segment of step-index MMF [100 m length, core (cladding) diameter is 105 μm (125 μm), and the numerical aperture is 0.22] to form the self-modulated laser speckles for subsequent imaging applications.

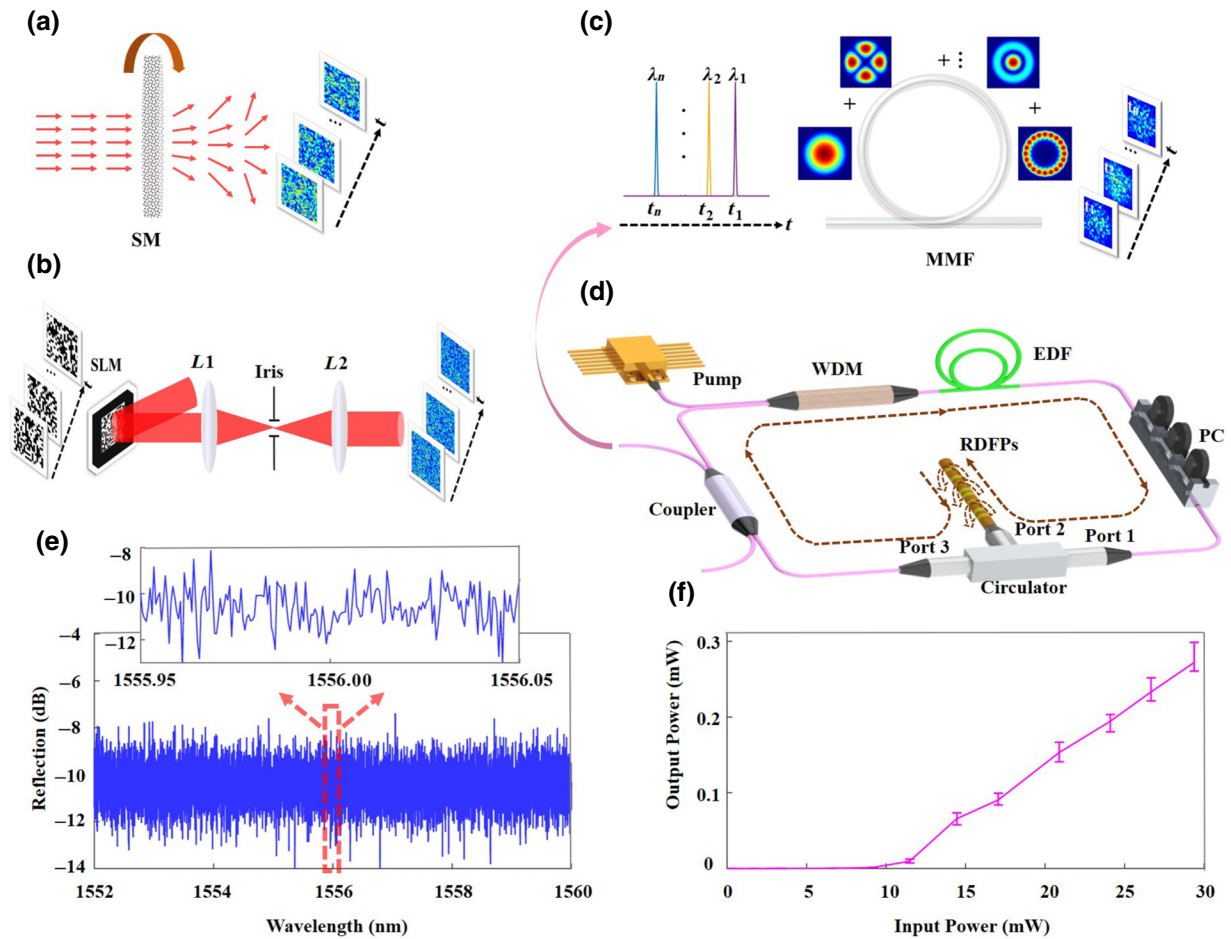


FIG. 1. Ways to generate spatiotemporally varied illumination speckle and schematic of the MDFL. (a) Coherent laser transmitting through a time-variant scattering medium. (b) Light field modulated by a spatial light modulator. (c) Mapping randomness from the spectral to spatial domain using a multimode fiber. (d) Experimental setup of the MDFL. (e) Reflection spectrum of the randomly distributed Fabry-Perot cavity array. Inset shows the enlargement of the reflection spectrum with a central wavelength of 1556 nm and bandwidth of 0.1 nm. (f) Output power of the MDFL versus the pump power. SM, scattering medium; L_1 , lens 1; L_2 , lens 2; WDM, wavelength-division multiplexer; EDF, erbium-doped fiber; RDFP, randomly distributed Fabry-Perot cavity; PC, polarization controller.

Due to the gain selection and strong mode competition, only a few of the eigenmodes can emit randomly, generating narrow-linewidth lasing with dynamically varying wavelength(s), as marked by different colors in Fig. 2(a). The spectra show sparse and randomly located sharp peaks, which are essential to form high-contrast time-variant speckles at the output end of the MMF. Figure 2(b) gives the laser's spectral distribution under a pump power of 11.51 mW by integrating 2000 spectra taken at different time slots, which reflects that the random lasing wavelengths are distributed over about 4-nm bandwidth. As discussed in the Sec. III, this bandwidth is within the decorrelation bandwidth of the opaque scattering medium, which retains the “memory” effect [24] of the scattering medium to recover hidden images. The integrated spectrum has no obvious correspondence with the reflection spectrum of Fig. 1(e), as shown in Fig. S3 within

the Supplemental Material [23]. This phenomenon can be attributed to two main reasons. First, since the reflection spectrum and the integrated spectrum are measured by two systems, there must be systematic error of the frequencies, which would lead to the mismatch. Second, the RDFP array is also sensitive to environmental vibrations and temperature changes, which would lead to a frequency shift of the reflection spectrum. Due to the limited number of random resonant cavities and the limited number of recorded spectra for statistics, there are some prominent emission frequencies, as shown in Fig. 2(b). In this case, the requirement of the application, as described in Ref. [21], is not fully satisfied, where all frequencies are supposed to be excitable equally to obtain the best performance of measurement. However, benefiting from the strong resonant-mode competition, the wavelength fluctuation is enough for the following application in terms of the

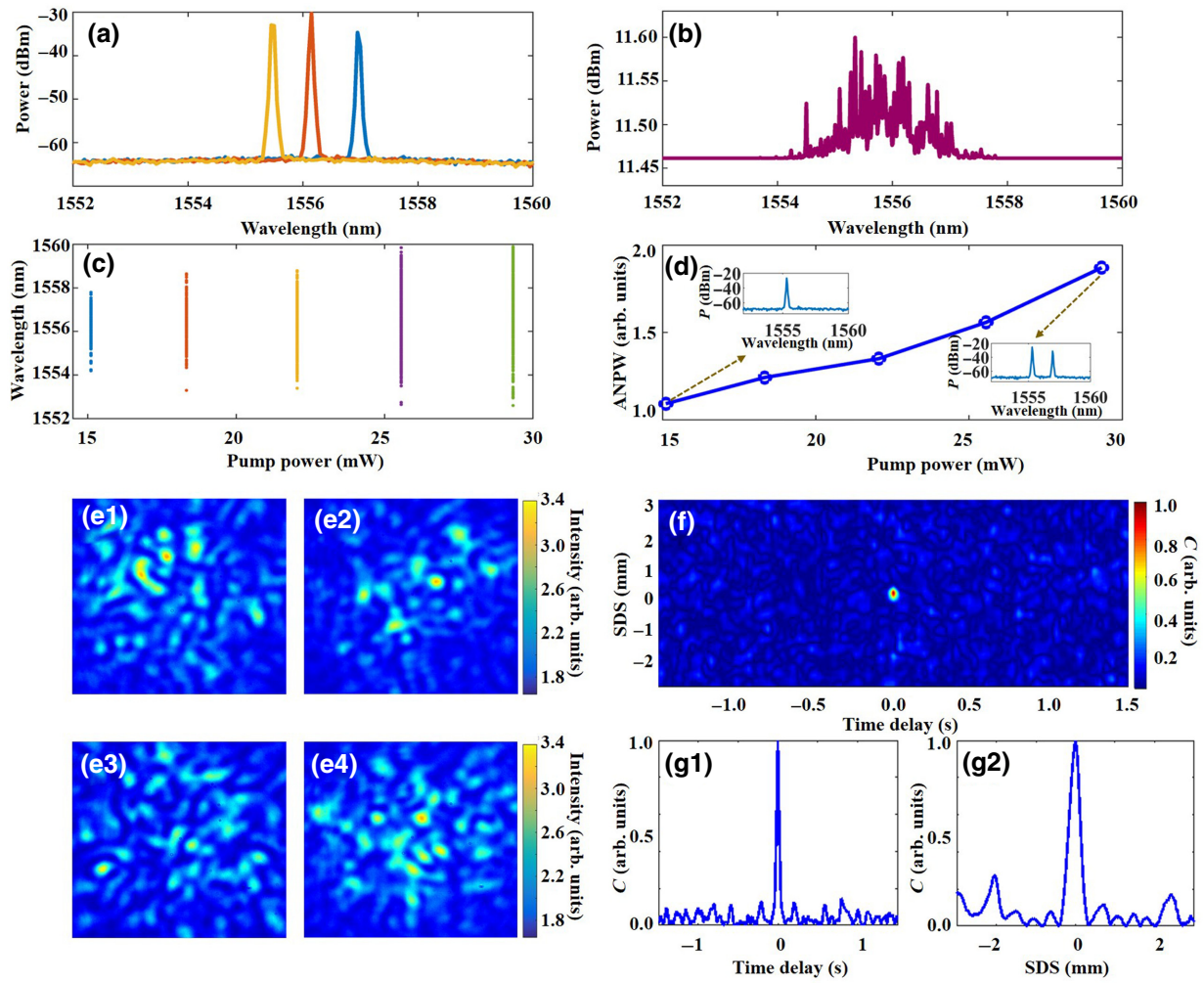


FIG. 2. Output characteristics of the MDFL. (a) Output spectra recorded at different moments under a pump power of 11.51 mW. (b) Time-integrated spectral distribution of the output spectra. (c) Statistical peak-wavelength distribution taken at 1000 successive moments versus pump power. (d) Average numbers of peak wavelength versus pump power. (e1)–(e4) Typical output patterns at four different moments. (f) Spatiotemporal correlation of the output. (g1) Temporal correlation when the spatial mismatch is zero. (g2) Spatial correlation when the temporal mismatch is zero. P , power; ANPW, average number of peak wavelength; SDS, spatial distance shift; C , correlation.

measured decorrelation time. The statistical wavelength distribution of spectral peaks broadens with an increase in pump power, as shown in Fig. 2(c). Additionally, the average number of sparse peaks in the laser spectra also grows slightly with an increase in pump power, while remaining less than two, as indicated in Fig. 2(d). The sparse characteristic of the emission spectra can guarantee high contrast of the generated speckles.

In the MDFL, the time-variant output spectrum is mapped to dynamically varied spatial patterns, as shown in Figs. 2(e1)–2(e4). Apparently, the generated speckles are spatially uncorrelated. Figures 2(f) and 2(g) give the value of spatiotemporal correlation index, C , as a function of spatial mismatch, Δx , and temporal mismatch, Δt . The formula for C is discussed in Sec. VII. The spatial

correlation index, $C(0, \Delta x)$, and the temporal correlation index, $C(\Delta t, 0)$, reflect that the generated speckles have a spatial correlation length of about 0.32 mm and a temporal correlation length of about 40 ms. This spatial correlation index is measured in the far field after being collimated by a lens, as shown in Fig. 4. The temporal correlation length is a proper value to match our camera, the largest frame rate of which is 100 frames/s. The temporal correlation length can be reduced by optimizing the structure of the coherent random-fiber laser. For example, by changing the feedback delay and feedback strength of the RDPFs, a greater number of eigenmodes that share similar net gains and possess similar Q values in the random resonant cavities can lead to stronger mode competition, which will reduce the decorrelation time of speckles. Considering

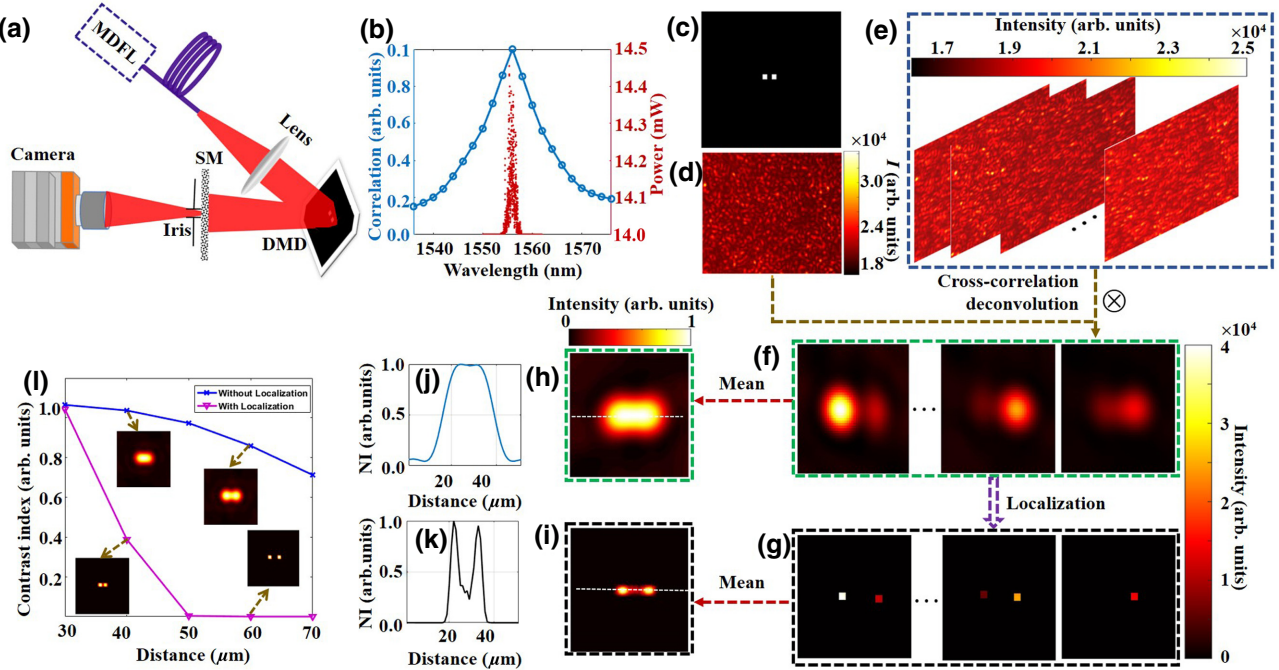


FIG. 3. Superresolution imaging using the MDFL. (a) Experimental setup. (b) Speckle decorrelation bandwidth of the opaque scattering medium (circle) and statistic on peak-wavelength distribution of the MDFL (dot). (c) Two rectangles serve as the object. (d) PSF of the imaging system. (e) Object speckles corresponding to different patterns of illumination. (f) Reconstructed patterns without localization. (g) Reconstructed patterns with localization. (h) Mean image of 1000 reconstructed patterns without localization. (i) Mean image of 1000 reconstructed patterns with localization. (j),(k) Intensity profiles along with the white dashed line in (h),(i). (l) Simulated contrast index versus the distance of the object for the methods without (upper curve) and with localization (lower curve). DMD, digital micromirror device; SM, scattering medium; I , intensity; NI, normalized intensity.

the response speed of the camera, the structure parameter used here is appropriate. According to this spatiotemporal characteristic, uncorrelated speckles can be generated and multiplexed to achieve speckle-illumination imaging through an opaque scattering medium, as demonstrated in the following Secs. III and IV.

III. SUPERRESOLUTION IMAGING THROUGH OPAQUE SCATTERING MEDIUM BASED ON THE MDFL

Deconvolution is one efficient method to recover the image of an object that is hidden by a scattering medium. The object speckle (i.e., the diffused pattern of the image that transmits through the opaque medium), I , can be expressed as the convolution of the object, O , with the PSF (P) of the scattering medium [24–28]:

$$I = O * P, \quad (1)$$

where the symbol $*$ denotes the convolution operation. By taking a cross correlation between I and PSF, the original object pattern can be reconstructed based on the fact that the autocorrelation of PSF is approximately a delta (δ) function [29]:

function [29]:

$$\begin{aligned} I \otimes P &= (O * P) \otimes P, \\ &= O * (P \otimes P), \\ &\approx O * \delta = O, \end{aligned} \quad (2)$$

where the symbol \otimes denotes a correlation operation. Actually, grains of the PSF are not infinitely small, but are limited by the numerical aperture and operation wavelength of the system. The autocorrelation of the PSF is more like a Gauss function other than a perfect delta function. This characteristic is similar to the Airy spot of lens-based optical imaging that limits the resolution. For example, if the distance between two points of O is less than the bandwidth of the Gauss function, the reconstructed image cannot separate the two points. This determines the resolution limit of the former standard deconvolution method, i.e., the method corresponding to Eq. (2).

To overcome the resolution limit, we use the MDFL to generate illumination patterns and use a localization method similar to single-molecule localization microscopy to localize and shrink points of the image [30,31]. Thus, different illumination patterns can be used to reconstruct different points of the image. Beneficial from the randomly generated illumination patterns, the whole image can be

recovered through the ergodicity of the reconstructed points. This procedure can be expressed as

$$\begin{aligned} I_i \otimes P &= (O_i * P) \otimes P, \\ &= O_i * (P \otimes P), \\ &\approx O_i * \delta = O_i, \end{aligned} \quad (3)$$

$$O = \sum_i L(O_i) = \sum_i L(I_i \otimes P). \quad (4)$$

Equation (3) describes the procedure of deconvolution to reconstruct each of the speckle-illuminated objects, O_i . $O_i = OS_i$ reflects the partially lightened object (subset of the whole region, O), wherein S_i is the illumination pattern from the MDFL, which performs as a random spatial filter that lights up only part of the object. Equation (4) describes the procedure to recover the whole image through localization and summation. L is the localization operator, which makes only the peak regions or pixels nonzero. Because S_i is a disordered pattern generated randomly by the MDFL, the probability to light up two neighboring points of O by the same S_i is extremely low. Thus, each peak region corresponds to a single point other than overlapping of two neighboring points of the object. Using the standard

deconvolution method without localization, the two neighboring points will be recovered as one overlapping region, if they are beyond the resolution, while our method can recover the two points one by one through localization and summation, superresolution imaging can be realized.

The experimental setup is shown in Fig. 3(a). The collimated output from the MDFL is used to illuminate the digital micromirror device (DMD), which is programmed as the image object. The reflected light from the DMD is captured by a near-infrared camera (Xenics, Bobcat-640-GigE) after transmitting through a ground-glass diffuser that acts as the opaque scattering medium. The iris, which is close to the ground glass, is used to control the grain size of the PSF captured by the camera, i.e., to set a specific system resolution. First, the speckle decorrelation bandwidth of the opaque scattering medium is characterized by employing a wavelength-scanning laser, as shown by the circle-marked fitting curve in Fig. 3(b). The decorrelation bandwidth is found to be about 7 nm, which is wider than the statistics for the peak-wavelength distribution of the MDFL [marked by the red dots in Fig. 3(b)]. Therefore, the MDFL can be used to implement the methods of Eqs. (2) and (4).

The measured PSF is shown in Fig. 3(d). Two $60 \times 60 \mu\text{m}^2$ rectangles are loaded into the DMD, serving as the object, as given in Fig. 3(c). A series of object

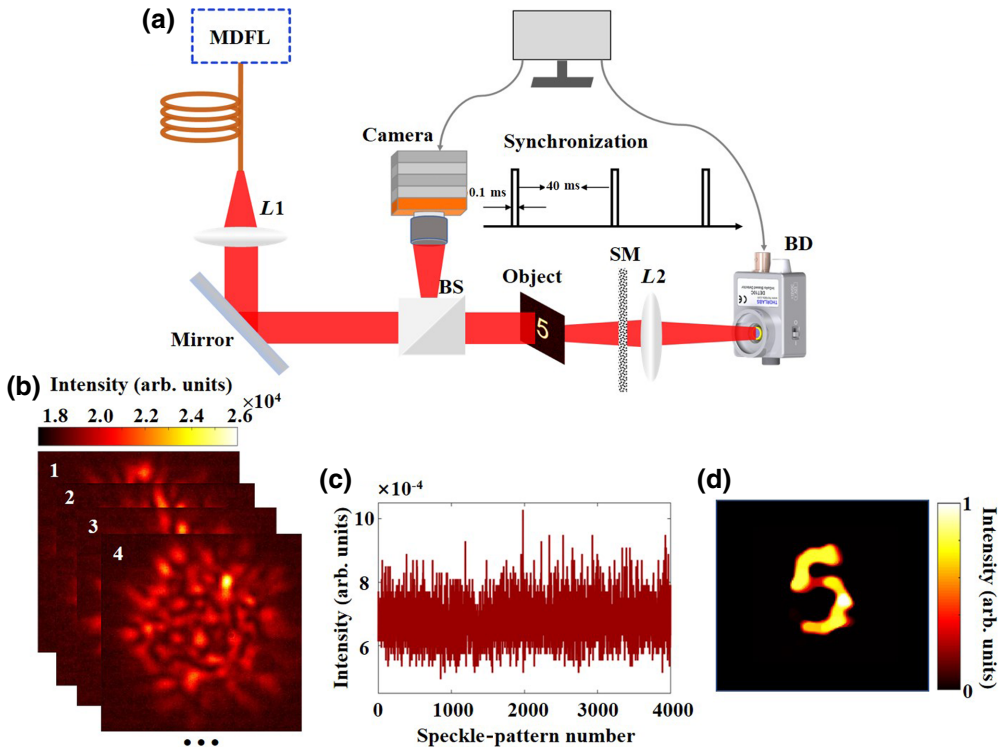


FIG. 4. Ghost imaging using the MDFL. (a) Schematic of the experimental setup. (b) Camera-recorded speckle patterns at different moments. (c) Data from the single-pixel detector. (d) Reconstruction of digit 5. L_1 , lens 1; BS, beam splitter; L_2 , lens 2; SM, scattering medium; BD, bucket detector.

speckles are taken periodically by the camera triggered by a gate signal with a period of 40 ms and a duty cycle of 0.05. A few of these object speckles, taken at different periods are shown in Fig. 3(e). Each of them corresponds to illumination by a specific output pattern of the MDFL.

Figure 3(f) gives the reconstructed images, O_i , that correspond to individual speckle illuminations. The whole image can be obtained by directly summing 1000 individual values of O_i , as shown in Fig. 3(h). It is equal to the imaging under uniform illumination (without localization), i.e., the standard deconvolution method based on Eq. (2). The two rectangles overlap with each other, and the high-frequency information of the object is missed, indicating that the system's resolution is not high enough. In parallel, the localization of each O_i is implemented to get the value $L(I_i \otimes \text{PSF}) = L(O_i)$, as shown in Fig. 3(g). The reconstructed image using Eq. (4) is given in Fig. 3(i), wherein two rectangles are clearly reconstructed. Figures 3(j) and 3(k) compare the intensity profiles along with the white dashed lines of Figs. 3(h) and 3(i), which further reflect that the imaging resolution can be improved by using the method of Eq. (4). That is, superresolution imaging through the opaque scattering medium is realized.

The relative size ratio, R , of the illumination speckle grains to the object influences the performance of the method given by Eq. (4), which is studied theoretically in Fig. 3(l). According to the experiment, the average size of illumination speckle grains is set to $40 \mu\text{m}$, and the diffraction limit of the imaging system is set to $60 \mu\text{m}$. In the simulation (see details in Sec. VII), the value of R can be varied by changing the distance between two rectangles. The contrast index (Γ) is defined to characterize the resolution, which is expressed as $\Gamma = 2I_{(r_1+r_2)/2}/(I_{r_1} + I_{r_2})$, where r_1 is the center position of the first rectangle and r_2 is the center position of the other one. The upper (lower) curve corresponds to the method without (with) localization, i.e., Eqs. (2) and (4). A smaller value of Γ reflects the better performance of imaging. Figure 3(l) reflects that the localization method can perform better when R is small. When R increases, especially when $R \geq 1$, the localization method cannot improve the imaging resolution, because the two rectangles will be simultaneously lightened up by the same grain of the illumination pattern. Thus, superresolution imaging through the opaque scattering medium can be realized if the illumination speckle grains are properly set.

IV. GHOST IMAGING USING THE MDFL

Spatial ghost imaging [32,33] requires spatiotemporal fluctuations of the illuminating field, which are usually realized by external modulation that leads to low lighting efficiency and bulky structures. Here, we use the proposed MDFL to generate all-fiber and automodulated laser speckles for illumination.

The experimental setup of ghost imaging is shown in Fig. 4(a). The structured output of the MDFL is collimated by a convex lens (L_1) and split by a beam splitter. The transmitted beam serves as signal light to illuminate the object (digit 5 in the USAF 1951 resolution chart) and is further collected by a single-pixel bucket detector (Thorlabs DET10C/M) through a $20\times$ objective (L_2). Ground glass is set between the object and the single-pixel detector, acting as an opaque scattering medium to verify the anti-jamming characteristic of the imaging. The reflective beam from the beam splitter serves as reference light, which is recorded by a camera that is deployed at the symmetrical plane of the object plane with respect to the beam splitter.

Data acquisition of the single-pixel detector and the camera are synchronized by a periodical gate signal. The period of the gate signal is set to be larger than 40 ms (from previous analysis of the temporal correlation) to ensure that the recorded speckles in each period are uncorrelated. Speckle patterns, A , captured by the camera and the corresponding voltage signals, y , detected by the single-pixel detector can be linked as

$$y^{m \times 1} = A^{m \times n} x^{n \times 1}, \quad (5)$$

where y is an m -dimensional column vector, representing the voltage values of m times measurements. A is an $m \times n$ matrix. Each row of A represents a vectorized illumination speckle corresponding to y . Information on the object is denoted by an n -dimensional row vector, x . In Eq. (5), $m \ll n$, so it is an underdetermined system of linear equations that has no unique solution. However, based on the sparsity feature of the natural object, the approximate solution can be extracted using the minimization of the gradient norm, as explained in Sec. VII.

Parts of data captured by the camera and the single-pixel detector are shown in Figs. 4(b) and 4(c), respectively. The speckle patterns are uncorrelated and the voltage signal fluctuates randomly in the temporal domain, which are typical characteristics of spatial ghost imaging. The reconstructed object is shown in Fig. 4(d), where digit 5 with a high signal-to-noise ratio is obtained, benefiting from the self-reconfigurable randomness of the MDFL.

V. DISCUSSION

Here, the dynamic variation of stimulated radiation wavelength may result from the following three mechanisms. First, the Kerr-type nonlinear shift of the refractive index can be excited under an appropriate laser power in a high- Q random cavity [34]. Second, since the laser is very sensitive to changes of the resonant cavity, disturbance from the environment, such as vibrations or temperature changes, is also a reason for the change in stimulated radiation wavelength [35]. Last, due to the existence of a large number of eigenmodes in the gain bandwidth of the EDF

and many of those eigenmodes sharing similar net gains, the competition between them can be fierce and will also lead to the change in stimulated radiation wavelength. So, any changes in the above three mechanisms will affect the stimulated radiation wavelength.

Different from previous methods of speckle-illumination generation (e.g., using rotating ground glass or a SLM), a dynamically varied speckle illumination is formed by combining the dynamic variation of the lasing wavelength of a coherent random laser with a multimode fiber, which has the advantages of an all-fiber structure, no moving parts, self-modulation, etc. This speckle-illumination method can potentially be used in some traditional speckle-illumination imaging, such as blind-structured illumination microscopy [4], ghost imaging [5], scattering-assisted imaging [6], and superresolution optical fluctuation imaging [7]. However, for imaging that strictly requires a stable laser wavelength (such as quantitative phase microscopy [36]), the proposed method is not applicable and the speckle-illumination methods using rotating ground glass or a SLM should be used.

VI. CONCLUSION

We propose and realize a spectrally, spatially, and temporally disordered fiber laser, i.e., the so-called multidimensionally disordered fiber laser. The laser emits randomly time-variant wavelengths to function as a simple, economic, and efficient wavelength-scanning source, and the wavelength randomness is mapped into the spatial domain by an integrated MMF, producing self-modulated speckle patterns that are preferred for speckle-illumination imaging. A method of imaging through an opaque scattering medium with superresolution ability is realized by making use of the intrinsic characteristics of the proposed laser and a localization strategy. That is, the ideas of speckle illumination and image localization are introduced into the deconvolution method, developing a localized deconvolution method to recover an image from an opaque scattering medium with better resolution than that of the standard deconvolution method. Additionally, spatial ghost imaging is also realized based on the illumination of the laser. This work provides an efficient tool and methods for imaging through an opaque scattering medium with improved performance, paving the way to advanced imaging for future applications in biomedicine and engineering.

VII. METHODS

The spatiotemporal correlation index, C , of the generated laser speckles is defined as [37]

$$C(\Delta x, \Delta t) = \frac{|\langle \delta I(x + \Delta x, t + \Delta t) \delta I(x, t) \rangle|}{\sqrt{\langle \delta I^2(x + \Delta x, t + \Delta t) \rangle \langle \delta I^2(x, t) \rangle}}, \quad (6)$$

where $\langle \cdot \rangle$ denotes the temporal average, $|\cdot|$ denotes the absolute value, Δx is the spatial mismatch, Δt is the temporal mismatch, and $\delta I(x, t) = I(x, t) - \langle I(x, t) \rangle$ represents the spatiotemporal fluctuation of emission intensity.

The simulation of our superresolution method is based on the Fresnel propagation theorem. First, the PSF is generated by considering a point propagation from the object plane to the image plane, which is expressed as [38]

$$P = \left| \iint_{\Sigma} e^{(ik/2u)(x_s^2 + y_s^2)} T(x_s, y_s) \text{circ} \times \left(\sqrt{x_s^2 + y_s^2}/d_0 \right) e^{(ik/2v)[(x_I - x_s)^2 + (y_I - y_s)^2]} ds \right|^2, \quad (7)$$

where the subscripts s and I denote the plane of scattering medium and image, respectively; r denotes the coordinate in transverse directions; u and v denote the object distance (the distance from the object plane to the image plane) and the image distance (the distance from the plane of the scattering medium to the image plane), respectively; T corresponds to the scattering medium, which is simplified as a pure phase mask [39]; circ denotes a circular hole function, representing the iris in the experiment; and the index d_0 is used to adjust the resolution of the system. The illumination speckles obey the Rayleigh statistics, which is generated by Fourier transform of a random phase distribution [40]:

$$S = F \left\{ \text{rand}(x, y) \text{circ} \left(\frac{\sqrt{x^2 + y^2}}{d_1} \right) \right\}, \quad (8)$$

where F denotes the Fourier transform and rand generates the random phase distribution between $-\pi$ and π . The index d_1 is used to adjust the size of speckle grains. Using the definitions of Eqs. (7) and (8), the deconvolution methods described by Eqs. (1)–(4) can be implanted numerically.

For our ghost imaging, the image can be extracted through minimization of the gradient norm:

$$\sum_i ||d_i x|| \quad \text{subject to } Ax = y, \quad (9)$$

where d represents the gradient operator, and $|| \cdot ||$ means a quadratic norm calculation. Here, we use the well-developed total-variation augmented Lagrangian alternating direction algorithm (TVAL3), which has advantages in fast reconstruction speed and high reconstruction quality. Detailed information on this algorithm can be found in Ref. [41].

The reflection spectrum of the RDFPs is measured by a wavelength-swept-laser-based optical spectrum analyzer

(OSA, Agilent with spectral resolution of 0.1 pm), as shown in Fig. S4 within the Supplemental Material [23]. The Agilent OSA consists of two parts: a tunable laser source (Agilent 81960A, resolution of 0.1 pm at 1550 nm) and an optical power meter (Agilent N7744A). So, it is based on an additional scanning light source to measure the reflection spectrum of the RDFFPs. The stimulated emission spectrum [Figs. 2(a)–2(d)] is measured by a grating-diffraction-element-based OSA (AQ6370D with a spectral resolution of 0.02 nm).

ACKNOWLEDGMENTS

This work is supported by the National Natural Science Foundation of China (NSFC) (Grants No. 11974071 and No. 61635005), the Guangdong Basic and Applied Basic Research Foundation (Grant No. 2020A1515111143), and the Sichuan Science and Technology Program (Grant No. 2020005). The authors thank Yaron Bromberg at the Hebrew University of Jerusalem for useful discussions and suggestions.

-
- [1] G. Vicedomini, P. Bianchini, and A. Diaspro, STED super-resolved microscopy, *Nat. Methods* **15**, 173 (2018).
- [2] X. Huang, J. Fan, L. Li, H. Liu, R. Wu, Y. Wu, L. Wei, H. Mao, A. Lal, and P. Xi, *et al.*, Fast, long-term, super-resolution imaging with Hessian structured illumination microscopy, *Nat. Biotechnol.* **36**, 451 (2018).
- [3] M. Pascucci, S. Ganesan, A. Tripathi, O. Katz, V. Emiliani, and M. Guillon, Compressive three-dimensional super-resolution microscopy with speckle-saturated fluorescence excitation, *Nat. Commun.* **10**, 1327 (2019).
- [4] N. Bender, M. Sun, H. Yilmaz, J. Bewersdorf, and H. Cao, Circumventing the optical diffraction limit with customized speckles, *Optica* **8**, 122 (2021).
- [5] E. Mudry, K. Belkebir, J. Girard, J. Savatier, E. Le Moal, C. Nicoletti, M. Allain, and A. Sentenac, Structured illumination microscopy using unknown speckle patterns, *Nat. Photonics* **6**, 312 (2012).
- [6] M. Leonetti, A. Grimaldi, S. Ghirga, G. Ruocco, and G. Antonacci, Scattering assisted imaging, *Sci. Rep.* **9**, 4591 (2019).
- [7] T. Chaigne, J. Gateau, M. Allain, O. Katz, S. Gigan, A. Sentenac, and E. Bossy, Super-resolution photoacoustic fluctuation imaging with multiple speckle illumination, *Optica* **3**, 54 (2016).
- [8] R. E. Meyers, K. S. Deacon, and Y. Shih, Turbulence-free ghost imaging, *Appl. Phys. Lett.* **98**, 111115 (2011).
- [9] R. E. Meyers, K. S. Deacon, and Y. Shih, Positive-negative turbulence-free ghost imaging, *Appl. Phys. Lett.* **100**, 131114 (2012).
- [10] A. M. Paniagua-Diaz, I. Starshynov, N. Fayard, A. Goetschy, R. Pierrat, R. Carminati, and J. Bertolotti, Blind ghost imaging, *Optica* **6**, 460 (2019).
- [11] F. Ferri, D. Magatti, A. Gatti, M. Bache, E. Brambilla, and L. A. Lugiato, High-Resolution Ghost Image and Ghost Diffraction Experiments with Thermal Light, *Phys. Rev. Lett.* **94**, 183602 (2005).
- [12] A. Haridas, S. M. Perinchery, A. Shinde, O. Buchnev, and V. M. Murukeshan, Long working distance high resolution reflective sample imaging via structured embedded speckle illumination, *Opt. Lasers Eng.* **134**, 106296 (2020).
- [13] Y. U. Lee, J. Zhao, Q. Ma, L. K. Khorashad, C. Posner, G. Li, G. B. M. Wisna, Z. Burns, J. Zhang, and Z. Liu, Metamaterial assisted illumination nanoscopy via random super-resolution speckles, *Nat. Commun.* **12**, 1559 (2021).
- [14] O. Katz, Y. Bromberg, and Y. Silberberg, Compressive ghost imaging, *Appl. Phys. Lett.* **95**, 131110 (2009).
- [15] L. Wang and S. Zhao, Fast reconstructed and high-quality ghost imaging with fast Walsh–Hadamard transform, *Photonics Res.* **4**, 240 (2016).
- [16] B. Redding, M. Alam, M. Seifert, and H. Cao, High-resolution and broadband all-fiber spectrometers, *Optica* **1**, 175 (2014).
- [17] G. D. Bruce, L. O’Donnell, M. Chen, M. Facchin, and K. Dholakia, Femtometer-resolved simultaneous measurement of multiple laser wavelengths in a speckle wavemeter, *Opt. Lett.* **45**, 1926 (2020).
- [18] R. Ma, Z. Wang, W. Y. Wang, Y. Zhang, J. Liu, W. L. Zhang, A. S. L. Gomes, and D. Y. Fan, Wavelength-dependent speckle multiplexing for imaging through opacity, *Opt. Lasers Eng.* **141**, 106567 (2021).
- [19] B. Redding, M. A. Choma, and H. Cao, Speckle-free laser imaging using random laser illumination, *Nat. Photonics* **6**, 355 (2012).
- [20] H. Zhu, W. Zhang, J. Zhang, R. Ma, Z. Wang, Y. Rao, and X. Li, Single-shot interaction and synchronization of random microcavity lasers, *Adv. Mater. Technol.* **6**, 2100562 (2021).
- [21] A. Boschetti, A. Taschin, P. Bartolini, A. K. Tiwari, L. Pattei, R. Torre, and D. S. Wiersma, Spectral super-resolution spectroscopy using a random laser, *Nat. Photonics* **14**, 177 (2019).
- [22] R. Ma, H. H. Zhang, E. Manuylovich, S. Sugavanam, H. Wu, W. L. Zhang, V. Dvoyrin, T. P. Hu, Z. J. Hu, and Y. J. Rao, *et al.*, Tailoring of spatial coherence in a multi-mode fiber by selectively exciting groups of eigenmodes, *Opt. Express* **28**, 20587 (2020).
- [23] See the Supplemental Material at <http://link.aps.org/supplemental/10.1103/PhysRevApplied.18.024031> for details of the RDFFPs, the actual experimental setup, the comparison between the integrated spectrum and the eigenmode frequencies, the experimental setup of measuring the eigenmode frequencies of RDFFPs, and change of reflectivity with the number of FC–PC-type fiber pigtails coated with gold film.
- [24] O. Katz, P. Heidmann, M. Fink, and S. Gigan, Non-invasive single-shot imaging through scattering layers and around corners via speckle correlations, *Nat. Photonics* **8**, 784 (2014).
- [25] T. F. Wu, O. Katz, X. P. Shao, and S. Gigan, Single-shot diffraction-limited imaging through scattering layers via bispectrum analysis, *Opt. Lett.* **41**, 5003 (2016).
- [26] S. K. Sahoo, D. Tang, and C. Dang, Single-shot multispectral imaging with a monochromatic camera, *Optica* **4**, 1209 (2017).

- [27] D. J. Wang, S. K. Sahoo, X. Zhu, G. Adamo, and C. Dang, Non-invasive super-resolution imaging through dynamic scattering media, *Nat. Commun.* **12**, 3150 (2021).
- [28] D. Lu, M. Liao, W. He, G. Pedrini, W. Osten, and X. Peng, Tracking moving object beyond the optical memory effect, *Opt. Lasers Eng.* **124**, 105815 (2020).
- [29] L. Li, Q. Li, S. Sun, H. Z. Lin, W. T. Liu, and P. X. Chen, Imaging through scattering layers exceeding memory effect range with spatial-correlation achieved point-spread-function, *Opt. Lett.* **43**, 1670 (2018).
- [30] M. J. Rust, M. Bates, and X. Zhuang, Sub-diffraction-limit imaging by stochastic optical reconstruction microscopy (STORM), *Nat. Methods* **3**, 793 (2006).
- [31] E. Betzig, G. H. Patterson, R. Sougrat, O. W. Lindwasser, S. Olenych, J. S. Bonifacino, M. W. Davidson, J. Lippincott-Schwartz, and H. F. Hess, Imaging intracellular fluorescent proteins at nanometer resolution, *Science* **313**, 1642 (2006).
- [32] W. Gong, C. Zhao, H. Yu, M. Chen, W. Xu, and S. Han, Three-dimensional ghost imaging lidar via sparsity constraint, *Sci. Rep.* **6**, 26133 (2016).
- [33] W. Gong and S. Han, High-resolution far-field ghost imaging via sparsity constraint, *Sci. Rep.* **5**, 9280 (2015).
- [34] Y. Bliokh, E. I. Chaikina, N. Lizárraga, E. R. Méndez, V. Freilikher, and F. Nori, Disorder-induced cavities, resonances, and lasing in randomly layered media, *Phys. Rev. B* **86**, 054204 (2012).
- [35] E. Chaikina, I. D. Vatnik, and D. V. Churkin, in *Fiber Lasers and Glass Photonics: Materials through Applications*, edited by S. Taccheo, J. I. Mackenzie, and M. Ferrari (SPIE, Strasbourg, 2018), p. 20.
- [36] Y. Choi, T. D. Yang, K. J. Lee, and W. Choi, Full-field and single-shot quantitative phase microscopy using dynamic speckle illumination, *Opt. Lett.* **36**, 2465 (2011).
- [37] K. Kim, S. Bittner, Y. Zeng, S. Guazzotti, O. Hess, Q. J. Wang, and H. Cao, Massively parallel ultrafast random bit generation with a chip-scale laser, *Science* **371**, 948 (2021).
- [38] R. Ma, Z. Wang, E. Manuylovich, W. L. Zhang, Y. Zhang, H. Y. Zhu, J. Liu, D. Y. Fan, Y. J. Rao, and A. S. L. Gomes, Highly coherent illumination for imaging through opacity, *Opt. Lasers Eng.* **149**, 106796 (2022).
- [39] S. Schott, J. Bertolotti, J. F. Leger, L. Bourdieu, and S. Gigan, Characterization of the angular memory effect of scattered light in biological tissues, *Opt. Express* **23**, 13505 (2015).
- [40] Y. Bromberg and H. Cao, Generating Non-Rayleigh Speckles with Tailored Intensity Statistics, *Phys. Rev. Lett.* **112**, 213904 (2014).
- [41] C. Li, W. Yin, and Y. Zhang, “Users Guide for TVAL3: TV Minimization by Augmented Lagrangian and Alternating Direction Algorithms,” CAAM Report, (2009)
- [42] M. Gagné and R. Kashyap, Demonstration of a 3 mW threshold Er-doped random fiber laser based on a unique fiber Bragg grating, *Opt. Express* **17**, 19067 (2009).

Correction: Captions and citations in text to Figures 3 and 4 were erroneously switched during the proof production process and have now been fixed. A minor error in Eq. (8) has been corrected.